Ceramics International 48 (2022) 24462–24470

Contents lists available at ScienceDirect

Ceramics International

journal homepage: www.elsevier.com/locate/ceramint

# Rietveld analysis and mechanical properties of in situ formed La-$\beta$-$Al_2O_3$/$Al_2O_3$ composites prepared by sol-gel method

Pedro Rivero-Antúnez [a,b,*], Víctor Morales-Flórez [a,b], Francisco Luis Cumbrera [a], Luis Esquivias [a,b]

[a] Departamento de Física de la Materia Condensada, Universidad de Sevilla, Sevilla, 41012, Spain
[b] Instituto de Ciencia de Materiales de Sevilla, Centro Mixto CSIC-Universidad de Sevilla, Sevilla, 41092, Spain

ARTICLE INFO

*Keywords:*
Alumina
Reinforced ceramics
Boehmite
Ceramic matrix composites
LaAl11O18
Rietveld

ABSTRACT

In this work, the crystal evolution of $\alpha$-$Al_2O_3$ composites reinforced with LBA platelets were monitored by XRD Rietveld. In addition, the mechanical properties of totally densified specimens were researched by Vickers and Knoop indentations. These composite materials were prepared by a sol-gel process from alumina seeded boehmite sol and lanthanum nitrate. X-ray diffraction data have been studied by Rietveld refinements and line profile analyses, paying attention to the LBA formation, the evolution of vol%, and crystallite size of the different phases. It has been observed that the appearance of the LBA phase happens at a lower temperature than in samples prepared by a conventional solid state reaction. Indentation tests revealed that the presence of LBA microplatelets in the sol-gel samples leads to a significant increase of their indentation fracture resistance, in comparison to the conventional samples.

## 1. Introduction

Resistance to chemical corrosion and wear, extreme hardness, or thermodynamic stability even at high temperatures are the essential characteristics of alumina ceramics. However, they present a major limitation since catastrophic failure occurs under mechanical or thermal stress due to their low fracture toughness. This is a serious drawback when replacing metallic alloys in some structural applications in advanced technology. Over the last forty years, structural ceramics have been intensively studied, and the improvements on their mechanical reliability are still an open source of discussion [1,2]. In more recent years, considerable emphasis has been done on the fabrication of composites where the crack propagation can be deflected and slowed down. It is common to find ceramics reinforced with second phases that present a extremly low dimensionality, such as graphene platelets, nanotubes or fibers [3–5], but they are expensive, hard to mix homogeneously, and need pressure-assisted densification. In this context, the growth of anisotropic second-phase grains formed *in situ*, is being proposed as a profitable alternative for microstructural reinforcement [6–12], as this procedure enhances homogeneity of phases, and thermal stability and electrical insulating properties [13,14].

The microstructure of rare-earth/$Al_2O_3$ ceramic systems sintered at temperatures beyond the eutectic point depends on the nature of the additives [15,16]. When $La_2O_3$ is added to alumina, a solid state reaction occurs, and a layered hexagonal aluminate with a defective magneto-plumbite structure appears [17]: $LaAl_{11}O_{18}$, also known as lanthanum hexa-aluminate, La-$\beta$-alumina, or LBA. Ropp and Carroll [18] studied the kinetics of this reactions, reporting a two-step process: initially, at 800 °C, a perovskite-type aluminate ($LaAlO_3$) forms (reaction 1); at higher temperatures (>1400 °C), this aluminate slowly reacts with $Al_2O_3$ to form elongated LBA grains (reaction 2).

$$La_2O_3 + Al_2O_3 \rightarrow 2{\cdot}LaAlO_3 \quad (1)$$

$$LaAlO_3 + 5{\cdot}Al_2O_3 \rightarrow LaAl_{11}O_{18} \quad (2)$$

In a former paper [19], it was demonstrated how the development of the crystalline phases and the evolution of the microstructure are influenced by the processing route for 30 vol% $LaAl_{11}O_{18}/Al_2O_3$ composites. The sol-gel method restrains densification because the geometry of the platelets disfavors packing. This fact, combined with the inhibited alumina grain growth, lead to poor density for samples sintered at <1450 °C. However, shrinkage took place in a narrower temperature

* Corresponding author. Department of Condensed-Matter Physics, University of Seville, P.O. 1065, Seville, 41080, Spain.
*E-mail addresses:* privero@us.es (P. Rivero-Antúnez), vmorales@us.es (V. Morales-Flórez), fcumbreras@us.es (F.L. Cumbrera), luisesquivias@us.es (L. Esquivias).
*URL:* http://grupo.us.es/fqm393/ (V. Morales-Flórez).

https://doi.org/10.1016/j.ceramint.2022.05.058
Received 8 March 2022; Received in revised form 21 April 2022; Accepted 5 May 2022
Available online 10 May 2022

interval and the formation of LBA platelets occurs at lower temperature than by other preparation methods. Almost identical XRD patterns are obtained for all samples after heating at 1450 °C for 5 h, independently of the preparation method, but the relative phase concentration evolution does depend on the preparation routine. Therefore, it was concluded that the growth of platelets controlled the densification process.

A revision of the bibliographical background reveals that the first application of *in situ* formed anisometric $\beta$-alumina grains was for the fabrication of abrasive grits [20]: through the incorporation of small amounts of $La_2O_3$ into $Al_2O_3$ by coprecipitation, the microstructural uniformity and the formation of $LaAl_{11}O_{18}$ were improved. In 1992, Kang et al. [21] added different concentrations of $LaAl_{11}O_{18}$ for the fabrication of self-reinforced $\alpha$-$Al_2O_3$, obtaining an increase of fracture toughness from 2.5 to 3.5 MGf[1] when raising the content of $LaAl_{11}O_{18}$. In the same year, Chen et al. [22] achieved a peak of fracture toughness of 4.3 MGf for alumina composites reinforced with a 30 vol% of LBA. A few years later, Yasuoka et al. [23] reported high flexural strength and high fracture toughness (630 MPa and 6 MGf, respectively) for silica--doped 20 vol% LBA/$Al_2O_3$ composites. Since then, LBA as well as many other $\beta$-aluminate with elongated grain morphologies, have been used as reinforcements for ceramic compounds, such as $SrAl_{12}O_{19}$ or $LaMgAl_{11}O_{19}$ [22,24], as they may lead to improvements in strength and fracture toughness compared to monolithic ceramic [22,25].

In this work, the basic knowledge on the formation of LBA/$Al_2O_3$ composites and their structure is examined. The crystallization and densifying process were studied by rigorous Rietveld analyses of XRD patterns. The effect of the sol-gel method on the formation of the LBA platelets was researched, emphasizing their formation and the effect of the temperature. Finally, the role of LBA as a mechanical reinforcing agent in alumina matrix is discussed.

## 2. Materials and methods

### 2.1. Sample synthesis

Two batches of samples were prepared for this work: a series prepared by sol-gel route, and another one by solid state reaction. The preparation routes of the powders of these two types of samples are summarized as follows (full details can be found in Ref. [19]):

#### 2.1.1. Sol-gel route

Inspired in the steps of Kumagai et al. [26], a boehmite ($\gamma$-AlO(OH)) sol (Disperal Sol P2, *Condea*, Germany, crystallite size 4.5 nm, dispersed particle size 20 nm, viscosity 10 mPa·s) was dispersed at pH = 4.5, and slowly seeded with 1.75 wt% of 100 nm diameter pure $\alpha$-$Al_2O_3$ particles. The seeded sol and $La(NO_3)_3{\cdot}6H_2O$ (*Johnson Matthey Electronics*, Wayne, USA) were mixed resulting in a volume ratio $Al_2O_3$/LBA = 7/3. The mixture was stirred for 24 h at room temperature, and then heated at 80 °C until gellation occurred. The dried xerogel was milled in an alumina mortar, and the resulting powder was sieved to <354 $\mu$m. Pellets were uniaxially pressed at 70 MPa, in order to conform handleable pieces, and then cold isostatically pressed at 275 MPa. Finally, the green bodies were calcined at 750 °C for 2 h. This series of samples were named SG. The whole process is summarized in Fig. 1.

#### 2.1.2. Solid-state reaction

Despite the samples prepared by the previous sol-gel process also will involve a solid-state reaction during its later sintering, this second method is referred to as a solid-state reaction, as it consists of a standard mixing of $\alpha$-$Al_2O_3$ powders and a $La_2O_3$ precursor.

High-purity (>99.99%, particle diameter = 0.3 $\mu$m) $\alpha$-$Al_2O_3$ powder (Baikalox SM8, *Baikowski International Corp.*, Charlotte, USA) was dispersed in distilled water with $HNO_3$ (pH 3) in presence of high power ultrasound and a magnetic stirrer, leading to a slurry texture. La $(NO_3)_3{\cdot}6H_2O$ was poured to the $\alpha$-$Al_2O_3$ to yield a mixture of 30 vol% LBA and 70 vol% $\alpha$-$Al_2O_3$ (same ratio of SG series). The mixture was mechanically stirred for 24 h while it dried on a hot plate at 100°C. These powders were calcined in air at 750°C for 2 h, and hand-grounded in an alumina mortar before and after calcination. Finally, the calcined powders were uniaxially pressed at 160 MPa. The resultant series of samples was designated as SSR.

#### 2.1.3. Calcination and sintering

The mentioned calcination at 750 °C for 2 h ensured the elimination of traces and the transformation of the $La(NO_3)_3$ into $La_2O_3$. At the same time, in the SG samples, the boehmite releases the hydroxyl groups, going into transition aluminas. After this calcination, samples were sintered by conventional pressureless sintering at 60 °C/h, with several dwell times at different temperatures, from 1050 up to 1650 °C.

Finally, pure commercial $\alpha$-$Al_2O_3$ nanopowders (same powders than the used in SSR samples) were sintered as a reference sample also through conventional pressureless sintering procedure under the same conditions used for SSR samples.

### 2.2. Structural and chemical characterization

The shrinkage of the pellets during heating was specifically monitored by thermal mechanical analysis (TMA), performed at 300 °C/h up to 1500 °C, with a dwell time of 3 h at this temperature. Samples were pre-heated at 800 °C for 2 h before TMA. Phase development was characterized with this method, and also by XRD/Rietveld analyses performed on the different stages of sintering of the samples.

The densities of the samples were determined by geometry, or by Archimedes' method if density >92% of the theoretical density. Sintered samples were polished by conventional ceramographics methods [27] up to 1 $\mu$m diamond slurry, and thermally etched for the study of their microstructures by scanning electron microscopy (SEM).

The XRD data were obtained with a *Philips* PW-1800 diffractometer (40 kV, 30 mA) equipped with a graphite mono-chromator and an automatic system of step-scanning. The wavelength was the corresponding to the Cu $K_\alpha$ ($\lambda = 0.15483$ nm). The range $2\theta \in (20°, 80°)$ was scanned at steps of 0.02° and 10 s. The profiles were refined with a recent version of the program *FullProf* for Rietveld analysis. The modified Thompson-Cox-Hasting pseudo-Voigt function was assumed as profile shape function [28]. Initial values for the parameters of the structure were taken from the *Powder Diffraction File* database (International Centre for Diffraction Data). The scale factors were obtained from the relation of Hill and Howard [29] and the completion of Rietveld protocol of refinement, which takes account for structural, profile and global parameters. These factors were used for the determination of relative abundances.

The conventional agreement indices were below $R_{wp} = 13.7$, $R_e = 8.4$, $\chi^2 = 2.64$. The volume-weighted distribution of different particle sizes was determined with the aid of software *BREADTH*. This program implement the "double-Voigt" method [30,31], equivalent to the classical Warren-Averbach approach [32]. In such a way, the program evaluates the column-length distribution parallel to the reciprocal [hkl] direction by choosing a hkl reflection of the pure profile and its harmonics.

### 2.3. Mechanical characterization

Mechanical characterization was performed on samples densified at

[1] Based on Profs. C. Ramadas and A. R. Jadhav's suggestion, the use of the unit "griffith" (Gf) was proposed [4] in substitution of the awkward classical magnitude $Pa{\cdot}m^{1/2}$, where 1 Gf = 1 $Pa\,m^{1/2}$, as a tribute to the mechanical engineer Alan Arnold Griffith (1893–1963). Griffith was known in the field of fracture mechanics for his pioneering studies on the nature of stress and failure due to crack propagation in brittle materials.

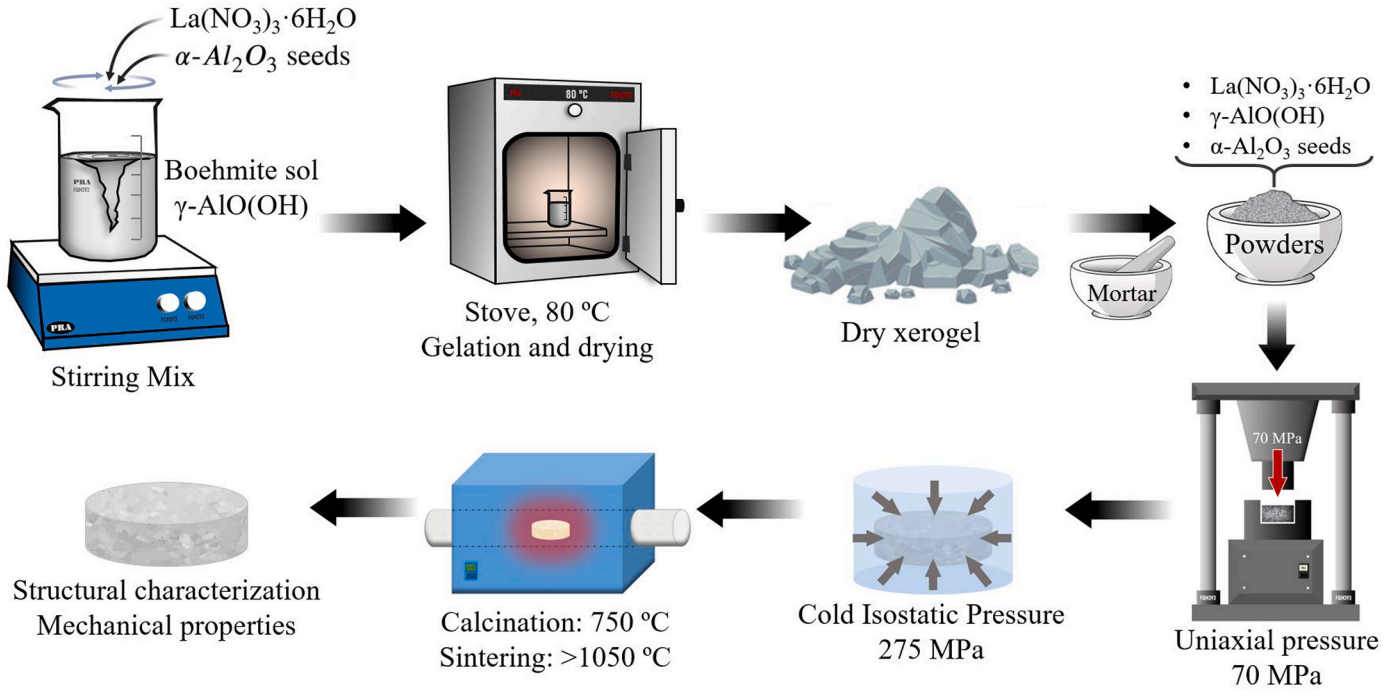


**Fig. 1.** Sketch summarizing the fabrication procedure of Sol-Gel samples.

1500 and 1600 °C. For the measurement of hardness, Vickers indentation tests were performed on mirror-finished surfaces. A load of 20 kp (196 N) was applied during a dwell time of 20 s using a *Buehler Wilson* VH1150 MicroVickers Hardness Tester. For the proper statistic treatment, the test was repeated at least ten times for each sample. Miyazaki et al. [33] proved that for dense alumina ceramics, Shetty's equation for median cracks [34] provides values of indentation fracture resistance ($K_{IFR}$) totally correlated with values of fracture toughness ($K_{Ic}$) measured by standardized methods, such as SEPB. Taking advantage of the Vickers indentation tests, the resultant radial cracks were measured, and $K_{IFR}$ was calculated to estimate the $K_{Ic}$, and elucidate differences between the toughness of the reference pure alumina sample and the composites. Shetty's equation for half-penny (median) cracks is expressed as follows:

$$K_{IFR} = 0.023(E/H)^{1/2} P \Big/ c^{3/2} \tag{3}$$

where $E$ is the Young's modulus, $H$ is the Vickers hardness, $P$ is the load applied by the tip, and $c$ is the length of the crack, measured from the center of the print. For the calculation of Young's modulus, Knoop indentations (load = 20 kp) were made in polished surfaces, and the procedure sugested by Marshall et al. [35] was followed. Given the geometry of the Knoop indenter, the relationship between the large diagonal ($D$) and the short diagonal ($d$) of the diamond tip is $D/d = 7.11$. However, after the indentation, the elastic recovery of the indented material shorten the length of the minor diagonal, whilst longer diagonal remains almost the same. Thus, when the unload is completed and the indenter is withdrawn, the ratio between the printed diagonals $d'/D'$, give us a way to measure the Young's modulus:

$$\frac{d'}{D'} \approx \frac{d'}{D} = \frac{d}{D} - \alpha \frac{H}{E} \tag{4}$$

$$\Rightarrow E = \frac{\alpha \cdot H}{1/7.11 - d'/D'} \tag{5}$$

where $\alpha = 0.45$ is a well known constant obtained from the fitting of several test performed on a wide type of ceramic materials [35], and $H$ is the hardness, obtained from Vickers tests.

## 3. Results and discussion

### 3.1. Structural evolution

#### 3.1.1. Rietveld analysis

In this work, Rietveld analyses were performed, so XRD data do not just give qualitative information about the existence of the different species, but we have also calculated the volume concentration of these phases and their grain size distributions, studying how those parameters evolve with the different sintering temperatures. In this sense, the qualitative description of the process was already reported in a previous paper, based on the first approach by XRD and SEM [19]. The results of volume concentrations and average grain sizes are summarized in Table 1.

As it was shown, in SSR samples, peaks of $LaAlO_3$ were not observed up to 1000 °C [19]. At 1050 °C $LaAlO_3$ represents a ~7 vol% (see Table 1). This phase increases its presence according to reaction 1 up to 10 vol%, at 1100 °C. At 1200<T ≤ 1250 °C, LBA appears [19]. Despite the onset of this transformation (reaction 2) is expected at T ~1250 °C, LBA does not represent a significant amount of the volume of the sample up to 1400 °C. At this temperature, $\alpha$-$Al_2O_3$ is the ~90 vol% of the sample, whereas perovskite $LaAlO_3$ still exists, meaning a 5.1 vol%, and LBA represents the 4.5 vol%. At 1500 °C, all the perovskite has been consumed and LBA jumps to be almost the 30 vol% of the composite, as planned during the preparation stage. With respect to the grain size of LBA, the average grain size ($d$) experiments a significant increase, from 90 nm at 1300 °C to 350 nm at 1650 °C (Table 1). Simultaneously, the grain size distribution becomes flatter, wider, and shifts to larger values (Fig. 2).

Regarding SG samples, it was reported that, at 750 °C, they are basically composed of $\gamma$-$Al_2O_3$ and incipient $\alpha$-$Al_2O_3$, without any signal of $LaAlO_3$, similar to the behavior of SSR samples. However, unlike SSR, $LaAlO_3$ was not found at 1000 °C in SG samples (although some $\gamma$-$Al_2O_3$ was present) [19]. It has been confirmed that, after 10 h at 1050 °C, a 3.5 vol% of perovskite appeared, as well as a 6.0 vol% of LBA (Table 1). Therefore, reaction 2 started at a temperature at least 200 °C lower than the required for SSR samples (Table 1). In Fig. 3, the identification of the

**Table 1**

Phase volume concentration (vol%) and crystallite average size ($d$) resulting from the Rietveld analysis of the X-ray diffraction patterns of the SSR and SG samples sintered at different temperatures.

| Sample | Phase | | 1050 °C | 1100 °C | 1150 °C | 1300 °C | 1350 °C | 1400 °C | 1500 °C | 1650 °C |
|---|---|---|---|---|---|---|---|---|---|---|
| **SSR** | $\alpha$-$Al_2O_3$ | vol% | 93.1 | 90.0 | | | | 90.4 | 72.7 | 72.9 |
| | | $d$ (nm) | | 240 | 260 | 290 | 290 | | | 370 |
| | $LaAlO_3$ | vol% | 6.9 | 10.0 | | | | 5.1 | 0.0 | 0.0 |
| | | $d$ (nm) | | 310 | | | | | | |
| | LBA | vol% | 0.0 | 0.0 | | | | 4.5 | 27.3 | 27.1 |
| | | $d$ (nm) | | | | 90 | 140 | 270 | | 350 |
| **SG** | $\alpha$-$Al_2O_3$ | vol% | 90.5 | 86.8 | 83.3 | 78.1 | 72.2 | 68.5 | 70.4 | 71.6 |
| | | $d$ (nm) | | 450 | | 480 | 510 | 540 | | 590 |
| | $LaAlO_3$ | vol% | 3.5 | 2.2 | 1.2 | 0.8 | 0.2 | 0.0 | 0.0 | 0.0 |
| | | $d$ (nm) | | 220 | | | | | | |
| | LBA | vol% | 6.0 | 11.0 | 15.5 | 21.1 | 27.6 | 31.5 | 29.6 | 28.4 |
| | | $d$ (nm) | | 240 | | | 430 | 440 | | 480 |

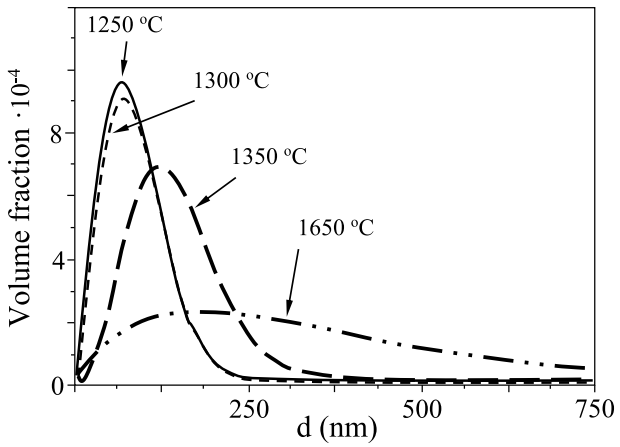


**Fig. 2.** Evolution of the volume fraction of LBA during sintering of SSR samples. La-$\beta$-aluminate crystallite size distribution for different sintering temperatures.

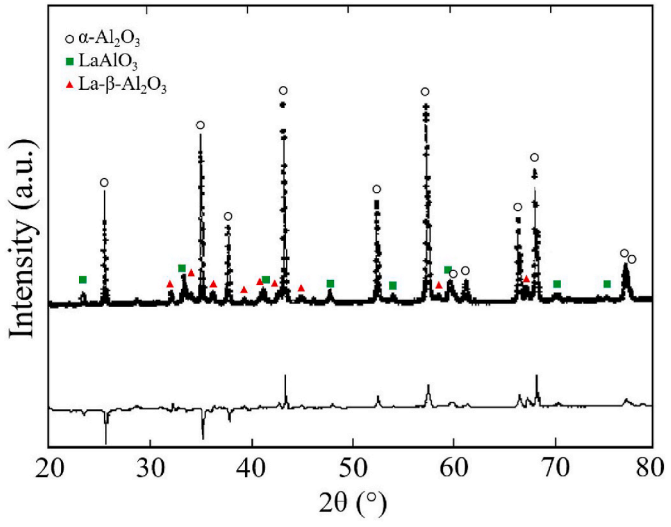


**Fig. 3.** Rietveld plot for diffraction data collected for SG sample heat-treated at 1050 °C during 10 h. The observed data are indicated by dots and the calculated pattern by the solid line overlying them. The line at the bottom of the pattern is the difference between the observed and calculated profile.

peaks and the fitting of the spectrum corresponding to the SG sample at 1050 °C can be seen. In addition, $LaAlO_3$ is present in a narrower range of temperatures: it appears at T ≤ 1050 °C, then it represents a 2.2 vol% at 1100 °C, and is rapidly consumed in the formation of LBA, with a residual content at 1300 °C (see Table 1).

The evolution of the grain size distribution of LBA in SG samples is shown in Fig. 4. The distributions do not reach the same heights than in SSR, but are wider, spanning over a wider range of grain sizes. In addition, the grain size distribution of SG suffers a less severe evolution than in the case of SSR samples (compare, e.g., the change in the average size or in the full witdh half maximum) given that in SG samples this phase is formed gradually since the first steps of sintering at lower temperatures in SG samples. Thanks to this faster reactivity, the ratio 7/3 of $\alpha$-$Al_2O_3$/LBA is reached quite earlier in samples prepared by sol-gel method.

In the composite samples, the alumina grain growth is inhibited by two mechanisms: on the one hand, the frictional (pinning) effect of LBA platelets with the migrating grain boundaries, which opposes to grain movements [36]; on the other hand, $La^{3+}$ cations segregate at grain boundaries, increasing the Al–O ionic bonding at grain boundaries, decreasing grain boundary diffusivities [37], and hindering the transformation of transition aluminas into $\alpha$-$Al_2O_3$ [38].

The precipitation of LBA has been also confirmed by SEM analysis. In

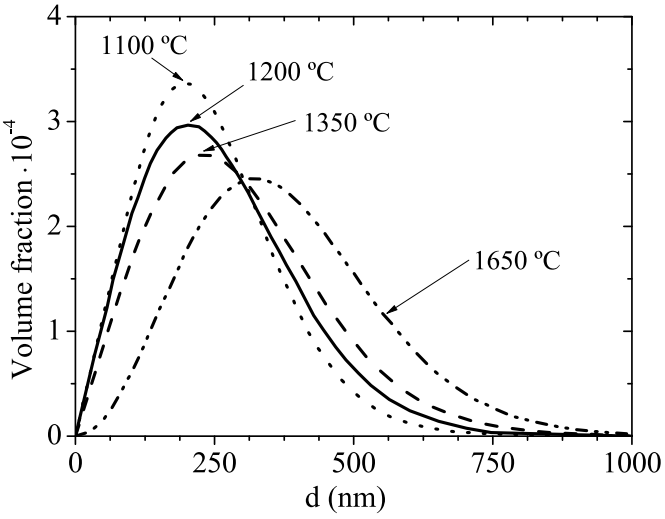


**Fig. 4.** Evolution of the volume fraction of LBA during sintering of SG samples. LBA crystallite size distribution for different sintering temperatures.

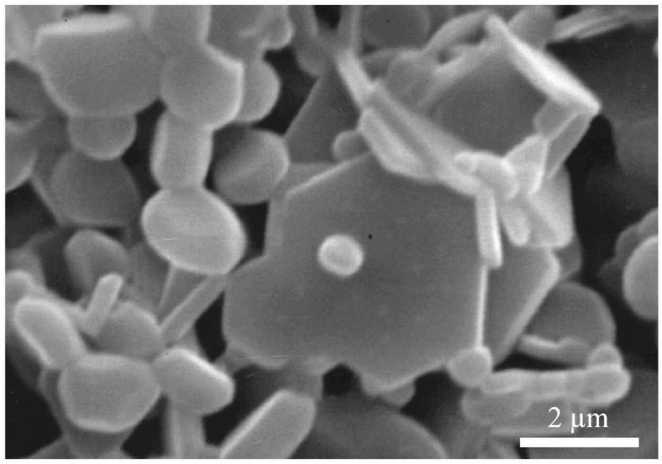


**Fig. 5.** Evidence of platelet-like structure of the anisometric phase LBA. Micrograph corresponding to the SG sample sintered at 1050 °C for 10 h.

the literature, LBA grains have been described as platelets [39–41], also referred as plate-like or needle-like, as well as barium or other rare-earth $\beta$-aluminate ceramic systems [15,25]. SEM images taken on the sample calcined at 1050 °C certainly show the plate-like shape of the LBA grains, confirming the existence of LBA at this temperature only when samples are prepared via sol-gel (see Fig. 5-left). In accordance to the Rietveld results (Fig. 2), LBA platelets have not been observed by SEM in SSR samples calcined at temperatures below 1250 °C.

### 3.1.2. Thermal mechanical analysis

The TMA tests gives information about the temperatures and times required for the densification of the samples, as well as the temperatures at which phase transformations could happen. The data obtained from this analysis is represented in Fig. 6. The densification rate of pure $\alpha$-$Al_2O_3$ (green data, squares) started increasing at approximately 950 °C, decelerating at ~1300 °C, being completely null after 20 min at 1500 °C. The maximum shrinkage rate was found at T = 1350 °C (t = 250 min).

On the other hand, due to the presence of a second phase, SSR samples (red data, solid circles) required more time and temperature before the shrinkage started, and it does not occur until ~1275 °C are reached, almost coinciding with the transformation of perovskite into LBA. Thus, the precipitation of the perovskite occurs without densification. The densification stopped some later than pure $\alpha$-$Al_2O_3$, 35 min after 1500 °C were reached, when all the $LaAlO_3$ has reacted.

As the samples were calcined at 750 °C before TMA analysis, the boehmite of SG suffered an endothermic transformation into $\gamma$-$Al_2O_3$, as expected from the evolution of transition aluminas [42], and its associated loss of mass and contraction. During the TMA (blue data, triangles), a first shrinkage started around 950 °C and stopped at ~1250 °C due to the transformation of transition aluminas (mostly $\gamma$-$Al_2O_3$) into $\alpha$-$Al_2O_3$. Note that shrinkage rate completely stopped (back to zero) before a second densification process started, revealing two well differentiated processes. This first step of densification suppose the transition from the density of $\gamma$-$Al_2O_3$ (3.65 g/cm$^3$ [43]) to the density of $\alpha$-$Al_2O_3$ (3.985 g/cm$^3$ [44]), an increase of 9.18%, thus, a theoretical shrinkage of 8.4% of the height of a cylindrical sample of fixed basal section, which coincides with the shrinkage that SG sample suffered during this first step of densification (area enclosed by the blue curve in Fig. 6 in the first step). Nevertheless, this coincidence is the result of two facts: not all the sample is made of alumina, and the $\alpha$-$Al_2O_3$ reached after this first step is not completely densified. Anyway, it can be considered as signature of the physics running in this process.

The next step of shrinkage occurs between 1350 °C and 1500 °C, and

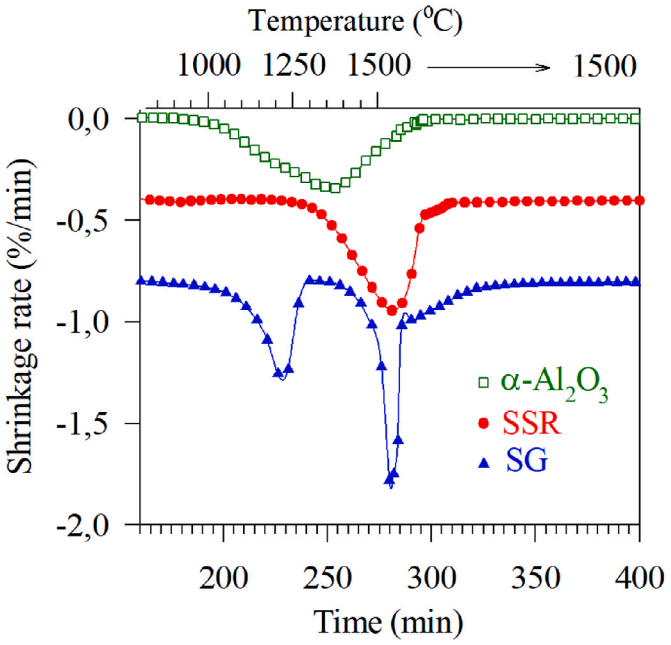


**Fig. 6.** Shrinkage behaviour versus temperature for heating ramp of 300 °C/h ( ~5 °C/min) and a 3 h dwell at 1500 °C. Samples were pre-heated at 800 °C for 2 h. The red circles and the blue triangles curves have been vertically shifted so they do not overlap at the origin. (For interpretation of the references to colour in this figure legend, the reader is referred to the web version of this article.)

it is due to the rearrangement and densification of $\alpha$-$Al_2O_3$, analogously to the densification of SSR and pure $\alpha$-$Al_2O_3$ samples, exhibiting the maximum shrinkage rate at exactly the same instant that in SSR sample: T = 1500 °C, t = 280 min. Thus, the presence of $La_2O_3$ and $LaAlO_3$ (precursors of LBA) is retarding the temperatures and times necessary for $\alpha$-$Al_2O_3$ densification.

Furthermore, in a sample of boehmite seeded with $\alpha$-$Al_2O_3$, those seeds play a crucial role accelerating the transformation of boehmite into $\alpha$-$Al_2O_3$, acting as nucleation sites, and reducing the required time and temperature [26,27]. This effect, nevertheless, is hindered in this sol-gel boehmite sample by the presence of LBA precursors. Schaper et al. [38] described that the sintering of alumina proceed via surface diffusion. This diffusion decreases by the formation of $LaAlO_3$ at the surface of alumina grains [45], postponing 100 °C the $\gamma \rightarrow \alpha$ phase transformation and the densification, results that are in complete agreement with those described in this work.

### 3.1.3. Sintering behavior and densification

The densities were measured for the determination of the composition and the level of densification. The densities are registered in Table 2 and in Fig. 7, expressed as the fraction of the theoretical density, i.e., 3,985 g/cm$^3$ for pure $\alpha$-$Al_2O_3$ [44], and 4.04 g/cm$^3$ for SG and SSR samples. This density is obtained by considering the theoretical 30 vol% of LBA (4.17 g/cm$^3$ [17]) present in these composites, supposing all the $LaAlO_3$ perovskite has reacted with alumina (reaction 2). Nevertheless, this criterion introduces an overestimation in the relative density of samples in stages in which they still contain $LaAlO_3$ (theoretical density = 6.53 g/cm$^3$ [46]) that has not reacted with $\alpha$-$Al_2O_3$ to form LBA. For example, a sample with a remaining 10 vol% of $LaAlO_3$ will show a relative density ~6% larger than the actual one.

At 1200 °C, the pure $\alpha$-$Al_2O_3$ sample is the most densified (73%), while the SSR sample is the least (53%). At this temperature, the SG sample is more densified (61%) than the SSR thanks to the first step of shrinkage observed at ~1150 °C in the TMA experiments, related to transition aluminas transforming into $\alpha$-$Al_2O_3$. This feature was explained in the previous section 3.1.2, but note that data cannot be

**Table 2**
Evolution of the densities of the samples, expressed as a fraction of the theoretical densities: 3.985 g/cm$^3$ for pure $\alpha$-$Al_2O_3$, and 4.04 g/cm$^3$ for SG and SSR composites.

| Temperature (°C) | 1100 | 1200 | 1250 | 1300 | 1400 | 1450 | 1500 | 1550 | 1650 |
|---|---|---|---|---|---|---|---|---|---|
| $\alpha$-$Al_2O_3$ | 0.65 | 0.73 | 0.81 | 0.93 | 0.98 | 0.98 | 0.98 | 0.99 | 0.99 |
| SSR | – | 0.53 | 0.57 | 0.72 | 0.90 | 0.92 | 0.94 | 0.95 | 0.99 |
| SG | – | 0.61 | 0.60 | 0.62 | 0.73 | 0.73 | 0.92 | 0.92 | 0.96 |

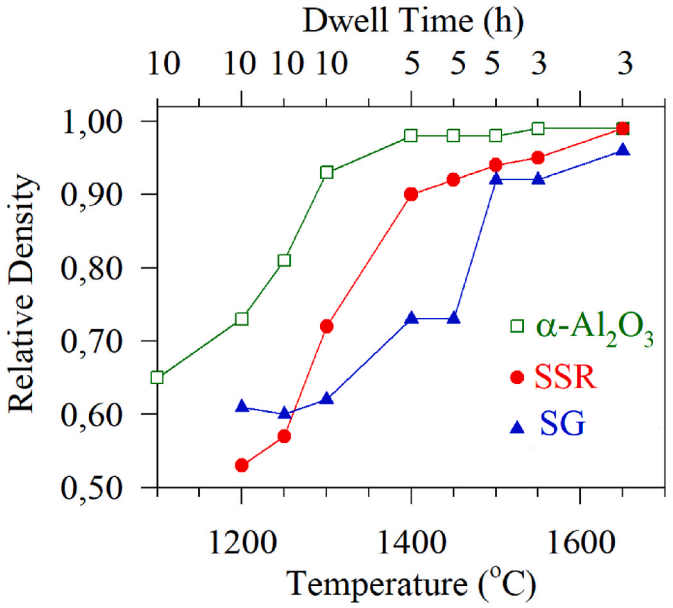


**Fig. 7.** Evolution of the densities of pure $\alpha$-$Al_2O_3$, SSR and SG samples for different temperatures and dwell times. Adapted with permission from Ref. [19].

completely correlated as density measurements were made at each indicated temperature after specific dwell times, while TMA were dynamic measurements. At 1300 °C, the differences between the samples becomes more pronounced: the pure $\alpha$-$Al_2O_3$ samples reaches 93% density at 1300 °C, while the SG sample is 61% dense, and the SSR is 71%. The formation of LBA platelets inhibits densification because their geometry disfavors packing. In SSR samples, LBA platelets appear at ~1250 °C and they form gradually. This slow appearing allows the rearrangement of particles, and subsequent densification. LBA represents just the 4.5 vol% at 1400 °C (Table 1), temperature at which the samples alredy exhibited a 90% of densification (Fig. 7 and Table 2). On the other hand, a significant amount of LBA platelets are alredy present in the SG sample since early stages, and their formation occurs rapidly, in a short interval. This fact hinders densification, allowing just a 73% of densification at 1400 °C. Notice that, at this temperature, pure $\alpha$-$Al_2O_3$ samples has already reached almost its maximum density.

In SSR sample, at ~1500 °C, when all the lanthanum has reacted and the vol. ratio LBA/$\alpha$-$Al_2O_3$ is 7/3, densities are in 94%, and densification continues till 99% after 3 h at 1650 °C, apparently unaffected by the existence of LBA platelets. On the other hand, the early appearance of anisometric structures in SG samples allows a major development of the platelets that reached bigger sizes (see Fig. 4), reducing the surface available for contact between particles during the sintering. This fact frustrates the densification: even after 3 h at 1650 °C, the SG sample did not obtain full density (Fig. 7 and Table 2).

The SEM micrographs reveal important differences between the samples after the treatment at the highest temperature of 1650 °C (Fig. 8). At this stage, pure $\alpha$-$Al_2O_3$ and SSR have obtained almost the 100% of theoretical densities, and SG the 96%. Given the large times and

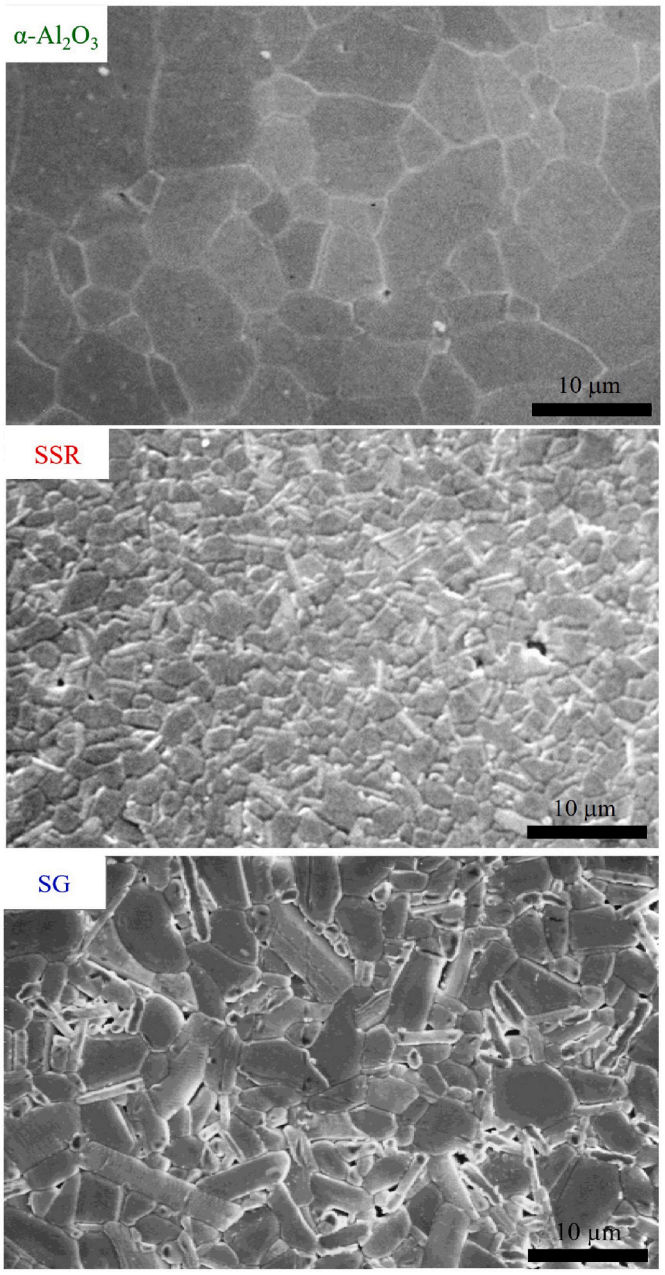


**Fig. 8.** SEM micrographs regarding the microstructures of samples sintered 3 h at 1650 °C. **Top**: fully dense comercial pure $\alpha$-$Al_2O_3$ sample. **Center**: fully dense SSR sample, exhibiting the finest structure. Adapted with permision from Ref. [19]. **Bottom**: SG sample, with a coarser grain structure and not fully densified (96%). Adapted with permision from Ref. [19].

temperatures of sintering, the grains of the pure $\alpha$-$Al_2O_3$ samples grew considerably. SSR exhibited the finest structure, while SG sample showed the larger platelets that obstructed rearrangement of particles, forced the densification to occur via grain growth, and resulted in a coarser microstructure. The apparent grain size of LBA observed by SEM confirms that the addition of LBA precursors reduces the ability to densify, as well as the alumina grain size. Note the discrepancies between SEM and XRD results regarding grain size that may arise from the fact that crystallite size (XRD) and grain size (SEM) are not the same. Finally, the homogeneous distributions of the LBA platelets can be also highlighted in the samples regarding SEM micrographies (Fig. 8).

### 3.2. Mechanical properties

The analysis of the mechanical properties of the different samples via Vickers and Knoop indentations allowed for the estimation of the Vickers Hardness, Young's modulus, and indentation fracture resistance, $K_{IFR}$ (results listed in Table 3). Firstly, there are not differences in the Vickers hardness of samples sintered at 1500 °C and 1650 °C. The highest value is achieved by the classical sample made of pure $\alpha$-$Al_2O_3$, as well as the largest value of Young's modulus, which are, besides, both in agreement with the values typically reported for fully dense $\alpha$-$Al_2O_3$ [22, 44]. On the other extreme, the sample with the lowest Vickers hardness is the SSR sample, despite it is fully dense at 1650 °C. The Hall-Petch effect predicts an increase of hardness as grain size decreases, however, the low hardness of LBA (~9 GPa [22]) plays a critical role, reducing the hardness of composites samples when a 30 vol% of LBA is used.

Young's modulus suffers significant increase of ~30% in all samples due to the last calcination step, from 1500 °C to 1650 °C, being grain growth and densifying decisive elements. Nevertheless, when monolithic sample is compared with the composites, the reduction may be attributed to the lower value of Young's modulus of LBA (~230 GPa [22]). To sum up, both hardness and elastic modulus decreases ~20% when a 30 vol% of LBA platelets is intercalated within the alumina matrix, mainly due to intrinsic lower values of the LBA [22,47].

Regarding the fracture resistance, the reliability of indirect methods, such as the indentation-based crack resistance, to estimate the fracture toughness or ceramics is widely discussed. Eventhough many authors claim that $K_{IFR}$ gives a good estimation of $K_{Ic}$ [33,48], these works are focused on fully dense ceramics, which is not exactly the case of SG sample sintered at 1500 °C nor 1650 °C (densification = 96%). In that case, densification may occur below the indenter, compromising the results. Nevertheless, we can find many works focused on LBA/$Al_2O_3$ systems which have reported an increase in fracture toughness measured by $K_{IFR}$ [22,49,50], as well as measured by standardized methods such as SEPB [23,51,52], all of them attributing the increase to crack deflection, a behavior also reported for other self-reinforced alumina matrix with elongated second phases [25].

The measured values of $K_{IFR}$ are shown in Table 3. Classical pure $\alpha$-$Al_2O_3$ sample showed the expected values, lower than those measured in SSR and SG samples. Thus, it can be inferred that the addition of LBA contributed to the increase of the indentation fracture resistance of the sample. In particular, sample SG exhibited the highest values of indentation fracture resistance, at 1500 °C and 1650 °C, an interesting result considering that it was less densified than the other samples in both cases. Two aspects may explain this feature: firstly, SG sample showed lower values of hardness; and, secondly, the existence of LBA platelets inhibited the growth of the matrix grains and led to a more tortuous path of the crack, helping to the dissipation of the energy of the crack through the crack deflection mechanism [23,49].

SEM images of the cracks (Fig. 9) revealed the increase of the path of the crack. On the top image, the big grains of the pure $\alpha$-$Al_2O_3$ sample allow the rapid propagation of the fracture. In the center and bottom images, LBA platelets can be easily distinguished by their brighter tonality due to their larger atomic mass. The smaller grains and the presence of the LBA platelets make more tortuous the intergranular crack path, leading to the observed increase of the indentation fracture resistance of the composite samples.

**Table 3**
Mechanical properties of the samples: Vickers Hardness (*HV*20), Young's modulus (*E*), and indentation fracture resistance ($K_{IFR}$).

| Sample | HV20 (GPa) | E (GPa) | $K_{IFR}$ (MGf) |
|---|---|---|---|
| **$\alpha$-$Al_2O_3$-1500** | 15.6 ± 0.2 | 350 ± 20 | 4.3 ± 0.7 |
| **$\alpha$-$Al_2O_3$-1650** | 16.1 ± 0.6 | 440 ± 30 | 5.1 ± 0.4 |
| **SSR-1500** | 11.1 ± 0.3 | 290 ± 20 | 4.9 ± 0.4 |
| **SSR-1650** | 11.3 ± 0.3 | 360 ± 20 | 5.6 ± 0.3 |
| **SG-1500** | 12.4 ± 0.7 | 280 ± 20 | 5.6 ± 0.3 |
| **SG-1650** | 12.0 ± 0.5 | 380 ± 10 | 6.5 ± 0.4 |

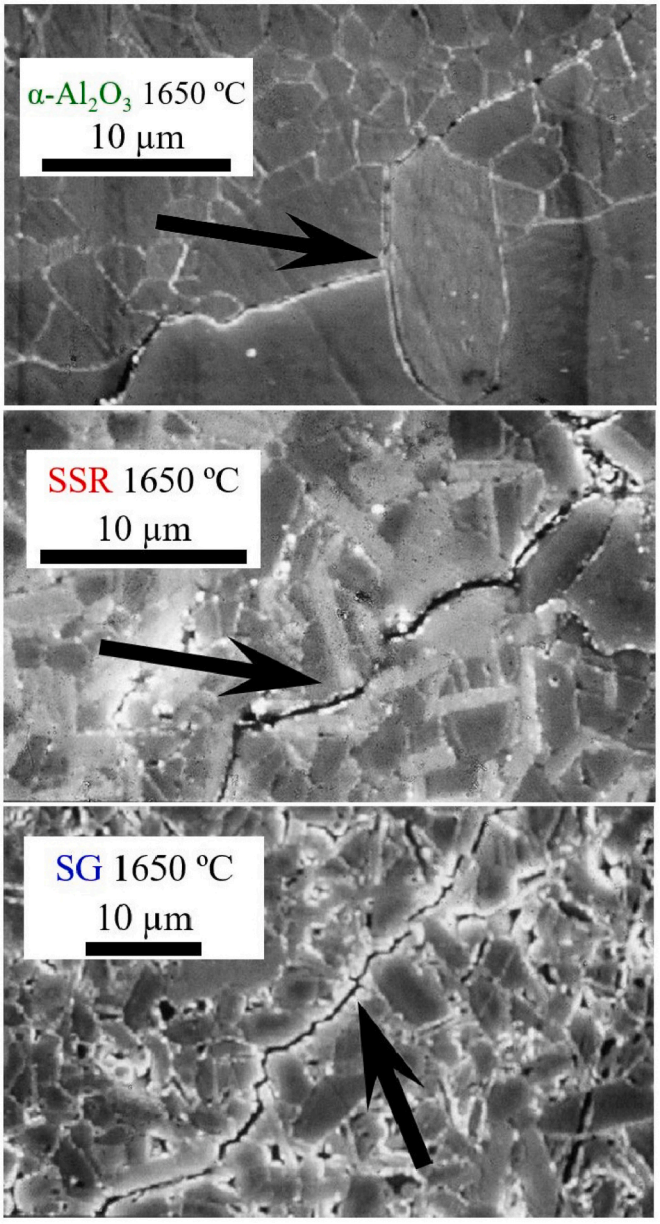


**Fig. 9.** Propagation of cracks produced after Vickers indentations on the different samples sintered at their max. Densities. The arrows show the crack paths.

## 4. Conclusions

The sol-gel method has been proven as an efficient method to enhance the precipitation of the LBA at lower temperatures than other solid-state reaction methods. Hence, as revealed by the Rietveld analyses and SEM imaging, LBA micrometric platelets were found in the sol-gel samples at temperatures as low as 1050 °C, 250 °C lower than in samples prepared by solid state reaction. Moreover, it was also observed that the growth of these platelets controls the densification process. Thus, the formation of platelets at low temperature, as it happens using the sol-gel method, restrains the densification because their geometry disfavours packing. This fact, combined with the inhibition of the alumina grain growth, involves a poor density for samples sintered at temperatures lower than 1450 °C in the sol-gel sample, and even impeded its full densification up to 1600 °C.

Finally, the influence of the homogeneous distribution of the LBA on the mechanical properties of the samples was assessed. In comparison to the pure alumina sample, LBA-alumina composites exhibited lower values of hardness and Young's moduli, but the indentation fracture resistance increased. This is specially significant in the case of the sol-gel sample, with an observed increase of 30% of the indentation fracture resistance.

## Declaration of competing interest

The authors declare that they have no known competing financial interests or personal relationships that could have appeared to influence the work reported in this paper.

## Acknowledgments

Project PGC2018-094952-B-I00 financed by *FEDER /Ministerio de Ciencia e Innovación - Agencia Estatal de Investigación - FEDER, UE*, and project P20-01121 financed by PAIDI2020 *Junta de Andalucia* are acknowledged. P. R-A acknowledge project PGC2018-094952-B-I00 from FEDER */Ministerio de Ciencia e Innovación - Agencia Estatal de Investigación*. The authors would like to thank the work by the National Institutes of Health, USA for the development of the *ImageJ* software.

## References

[1] V. Morales-Flórez, A. Dominguez-Rodriguez, Mechanical properties of ceramics reinforced with allotropic forms of carbon, Prog. Mater. Sci. (2021), https://doi.org/10.1016/j.pmatsci.2022.100966 (accepted).
[2] E. Zapata-Solvas, D. Gómez-García, A. Domínguez-Rodríguez, Towards physical properties tailoring of carbon nanotubes-reinforced ceramic matrix composites, J. Eur. Ceram. Soc. 32 (2012) 3001–3020.
[3] L. Esquivias, P. Rivero-Antúnez, C. Zamora-Ledezma, A. Domínguez-Rodríguez, V. Morales-Flórez, Intragranular carbon nanotubes in alumina-based composites for reinforced ceramics, J. Sol. Gel Sci. Technol. 90 (2019) 162–171.
[4] P. Rivero-Antúnez, R. Cano-Crespo, L. Esquivias, N. de la Rosa-Fox, C. Zamora-Ledezma, A. Domínguez-Rodríguez, V. Morales-Flórez, Mechanical characterization of sol-gel alumina-based ceramics with intragranular reinforcement of multiwalled carbon nanotubes, Ceram. Int. 46 (2020) 19723–19730.
[5] E. Zapata-Solvas, D. Gómez-García, A. Domínguez-Rodríguez, On the microstructure of single wall carbon nanotubes reinforced ceramic matrix composites, J. Mater. Sci. 45 (2010) 2258–2263.
[6] X. Xiong, Z. Wang, X. Wang, H. Liu, Y. Ma, Enhancing mechanical properties and air permeability of corundum porous materials by in situ formation of LaAl11O18 in bonding phase, J. Rare Earths 38 (2020) 195–202.
[7] S.A. Basha, K.S. Chandra, D. Sarkar, Salient features of SrO doping in Al2O3 – 5 wt. %ZrO2 reaction sintered composite ceramics, J. Alloys Compd. 829 (2020), 154559.
[8] L. Liu, Y. Takasu, T. Onda, Z.C. Chen, Influence of in-situ formed Ba-$\beta$-Al2O3 on mechanical properties and thermal shock resistance of ZTA/Ba-$\beta$-Al2O3 composites, Ceram. Int. 46 (2020) 3738–3743.
[9] Y.L. Xin, H.F. Yin, Y. Tang, H.D. Yuan, X.H. Ren, K. Gao, Q.F. Wan, Y.C. Liu, Formation mechanism of MgSrAl10O17 and its effect on the mechanical performance of lightweight Al2O3–MgAl2O4 refractories, Ceram. Int. 46 (2020) 11075–11079.
[10] A.P. Luz, J.H. Gagliarde, C.G. Aneziris, V.C. Pandolfelli, B4C mineralizing role for mullite generation in Al2O3-SiO2 refractory castables, Ceram. Int. 43 (2017) 12167–12178.
[11] J.-F. Tsai, U. Chon, N. Ramachandran, D.K. Shetty, Transformation plasticity and toughening in CeO2-partially-stabilized Zirconia-alumina (Ce-TZP/Al2O3) composites doped with MnO, J. Am. Ceram. Soc. 75 (1992) 1229–1238.
[12] P.F. Becher, Microstructural design of toughened ceramics, J. Am. Ceram. Soc. 74 (1991) 255–269.
[13] R.R. Rao, L. Mariappan, Combustion synthesis and characterisation of lanthanum hexa-aluminate, Adv. Appl. Ceram. 104 (2005) 268–271.
[14] R. Gadow, M. Lischka, Lanthanum hexaaluminate - novel thermal barrier coatings for gas turbine applications - materials and process development, Surf. Coating. Technol. 151–152 (2002) 392–399.
[15] J. Zhang, M. Fang, Z. Huang, Y.G. Liu, X. Min, X. Wu, Preparation and mechanical properties of ReAl11O18 ceramics, Key Eng. Mater. 602–603 (2014) 345–348.
[16] K. Hamano, S. Ohta, Y. Ozaki, Effects of rare earth oxides on sintering of alumina, J. Ceram. Soc. Jpn. 87 (1979) 632–641.
[17] N. Iyi, Z. Inoue, S. Takekawa, S. Kimura, The crystal structure of lanthanum hexaaluminate, J. Solid State Chem. 54 (1984) 70–77.
[18] R.C. Ropp, B. Carroll, Solid-state kinetics of LaAl11O18, J. Am. Ceram. Soc. 63 (1980) 416–419.
[19] C. Barrera-Solano, L. Esquivias, G.L. Messing, Effect of preparation conditions on phase formation, densification, and microstructure evolution in La-$\beta$-Al2O3/Al2O3 composites, J. Am. Ceram. Soc. 82 (1999) 1318–1324.
[20] W.P. Wood, L.D. Monroe, S.L. Conwell, Abrasive Grits Formed of Ceramic Containing Oxides of Aluminum and Rare-Earth Metal, Method of Making and Products Made Therewith, U.S. Pat. No. 4 881 951, Nov. 21, 1989.
[21] S.W. Kang, J.W. Ko, H.D. Kim, formation of La-beta-Aluminate in alpha-alumina matrix and its influence on mechanical properties, J. Kor. Chem. Soc. 29 (1992) 23–28.
[22] P.L. Chen, I.W. Chen, In-situ alumina/aluminate platelet composites, J. Am. Ceram. Soc. 75 (1992) 2610–2612.
[23] M. Yasuoka, K. Hirao, M.E. Brito, S. Kanzaki, High-strength and high-fracture-toughness ceramics in the Al2O3/LaAl11O18 systems, J. Am. Ceram. Soc. 78 (1995) 1853–1856.
[24] R.A. Cutler, R.J. Mayhew, K.M. Prettyman, A.V. Virkar, High-toughness Ce-TZP/Al2O3 ceramics with improved hardness and strength, J. Am. Ceram. Soc. 74 (1991) 179–186.
[25] Z.-C. Chen, S. Nugroho, M. Ezumi, T. Akao, T. Onda, In situ synthesis of alumina-matrix oxide/oxide composites by reactive sintering, Mater. Sci. Eng. 557 (2012) 59–68.
[26] M. Kumagai, G.L. Messing, Controlled transformation and sintering of a boehmite sol-gel by $\alpha$-alumina seeding, J. Am. Ceram. Soc. 68 (1985) 500–505.
[27] P. Rivero-Antúnez, R. Cano-Crespo, F. Sánchez-Bajo, A. Domínguez-Rodríguez, V. Morales-Flórez, Reactive SPS for sol–gel alumina samples: structure, sintering behavior, and mechanical properties, J. Eur. Ceram. Soc. 41 (2021) 5548–5557.
[28] P. Thompson, D.E. Cox, J.B. Hastings, Rietveld refinement of Debye–Scherrer synchrotron X-ray data from Al2O3, J. Appl. Crystallogr. 20 (1987) 79–83.
[29] R. Hill, C. Howard, B. Reichert, Quantitative phase Abundance in Mg-PSZ by Rietveld analysis of neutron and X-ray diffraction data, Mater. Sci. Forum 34–36 (1988) 159–163.
[30] D. Balzar, Breadth – a program for analyzing diffraction line broadening, J. Appl. Crystallogr. 28 (1995) 244–245.
[31] D. Balzar, X-ray diffraction line broadening: modeling and applications to high-Tc superconductors, J. Res. Natl. Inst. Stand.Technol. 98 (1993) 321.
[32] B.E. Warren, B.L. Averbach, The effect of cold-work distortion on x-ray patterns, J. Appl. Phys. 21 (1950) 595–599.
[33] H. Miyazaki, Y. Yoshizawa, A reinvestigation of the validity of the indentation fracture (IF) method as applied to ceramics, J. Eur. Ceram. Soc. 37 (2017) 4437–4441.
[34] D.K. Shetty, A.R. Rosenfield, W. Duckworth, Analysis of indentation crack as a wedge-loaded half-penny crack, J. Am. Ceram. Soc. 68 (1985). C–65–C–67.
[35] D.B. Marshall, T. Noma, A.G. Evans, A simple method for determining elastic-modulus–to-hardness ratios using Knoop indentation measurements, J. Am. Ceram. Soc. 65 (1982) c175–c176.
[36] Z. Negahdari, M. Willert-Porada, Tailoring the microstructure of reaction-sintered alumina/lanthanum hexaaluminate particulate composites, J. Eur. Ceram. Soc. 30 (2010) 1381–1389.
[37] H. Yoshida, S. Hashimoto, T. Yamamoto, Dopant effect on grain boundary diffusivity in polycrystalline alumina, Acta Mater. 53 (2005) 433–440.
[38] H. Schaper, E.B. Doesburg, L.L. Van Reijen, The influence of lanthanum oxide on the thermal stability of gamma alumina catalyst supports, Appl. Catal. 7 (1983) 211–220.
[39] T. Fujii, H. Muragaki, H. Hirano, Microstructure development and mechanical properties of Ce-TZP/La-$\beta$-Alumina composites, in: S. Hirano, G.L. Messing, H. Hausner (Eds.), Ceramic Powder Science IV, vol. 22, (Ceramic Transactions), American Ceramic Society, Westerville, OH, 1991, pp. 693–698.
[40] B.-K. Jang, T. Kishi, Fabrication and microstructure of Al2O3 matrix composites by in-situ reaction in the Al2O3-La2O3 system, J. Ceram. Soc. Jpn. 106 (1998) 739–743.
[41] P. Jana, P.S. Jayan, S. Mandal, K. Biswas, Effect of seeding on the formation of lanthanum hexaaluminates synthesized through advanced sol gel process, J. Cryst. Growth 408 (2014) 7–13.
[42] P. Souza-Santos, H. Souza-Santos, S. Toledo, Standard transition aluminas. Electron microscopy studies, Mater. Res. 3 (2000) 104–114.

[43] I. Levin, D. Brandon, Metastable Alumina polymorphs: crystal structures and transition sequences, J. Am. Ceram. Soc. 81 (1998) 1995–2012.
[44] F. Cardarelli, Materials Handbook, second ed., Springer London, London, 2008 https://doi.org/10.1007/978-1-84628-669-8.
[45] W. Huang, G. Liu, X. Li, T. Qi, Q. Zhou, Z. Peng, Structural variation in improving thermal stability of transition alumina with La dopant, J. Alloys Compd. 824 (2020) 153905.
[46] F.S. Galasso, Structure, Properties, and Preparation of Perovskite-type Compounds, first ed., Pergamon, Oxford, 1969 https://doi.org/10.1016/C2013-0-02117-2.
[47] Z. Negahdari, M. Willert-Porada, C. Pfeiffer, Mechanical properties of dense to porous alumina/lanthanum hexaaluminate composite ceramics, Mater. Sci. Eng., A 527 (2010) 3005–3009.
[48] H. Miyazaki, Y.I. Yoshizawa, Correlation of the indentation fracture resistance measured using high-resolution optics and the fracture toughness obtained by the single edge-notched beam (SEPB) method for typical structural ceramics with various microstructures, Ceram. Int. 42 (2016) 7873–7876.
[49] Y.Q. Wu, Y.F. Zhang, X.X. Huang, J.K. Guo, In-situ growth of needlelike LaAl11O18 for reinforcement of alumina composites, Ceram. Int. 27 (2001) 903–906.
[50] Y.Q. Wu, Y.F. Zhang, X.X. Huang, B.S. Li, J.K. Guo, Preparation, sintering and fracture behavior of Al2O3/LaAl11O18 ceramic composites, J. Mater. Sci. 36 (2001) 4195–4199.
[51] I. Yamashita, K. Tsukuma, T. Kusunose, Translucent Al2O3/LaAl11O18 composite, J. Am. Ceram. Soc. 92 (2009) 2136–2138.
[52] M. Yasuoka, K. Hirao, M.E. Brito, S. Kanzaki, Microstructure and mechanical properties of alumina based ceramics with changed amounts of $\beta$-lanthanaluminate, J. Ceram. Soc. Jpn. 105 (1997) 641–644.